minerals

MDPI

Article

Occurrence Characteristics of Lead–Zinc Mine and Low-Flying Aeromagnetic Prospecting in a Forested Region of Yichun City

Naixuan Ji [1], Xiaoxiao Qin [1], Heyu Wu [2], Zi Wang [3], Wei Du [1,*], Yun Liu [1], Tiehan Zhang [1], Shengze Zhang [4] and Qiaomu Shi [5]

[1] School of Earth Sciences, Yunnan University, Kunming 650500, China; jinaixuan@stu.ynu.edu.cn (N.J.); qinxiaoxiao@stu.ynu.edu.cn (X.Q.); yunliu@ynu.edu.cn (Y.L.); zhangtiehan@stu.ynu.edu.cn (T.Z.)
[2] College of Geo-Exploration Science and Technology, Jilin University, Changchun 130026, China; wuhy18@mails.jlu.edu.cn
[3] State Key Laboratory of Petroleum Resources and Prospecting, China University of Petroleum, Beijing 102200, China; wangzi_ah@163.com
[4] Urumqi Branch, Geophysical Research Institute, Bureau of Geophysical Prospecting, China National Petroleum Corporation, Urumqi 830000, China; zsz1996916@163.com
[5] PetroChina Jilin Oilfield Company, Songyuan 138000, China; 15764423216@163.com
* Correspondence: duwei@ynu.edu.cn

Abstract: Understanding the characteristics of lead–zinc mine occurrences and mastering effective investigative techniques are paramount in modern ore prospecting. This research focuses on the forested region of Yichun city in China, with a specific emphasis on the strategic mineral resource of a lead–zinc mine. The study examines the distribution patterns of this mineral and employs advanced aeromagnetic exploration methods. Firstly, we analyzed the geological structure and features of the region by leveraging the latest high-precision aeromagnetic data collected using dynamic delta wing technology. This analysis was complemented by an assessment of the geological conditions of the research area, existing lead–zinc deposits, ground magnetic surveys, and verification studies. With the goal of establishing a meaningful correlation between aeromagnetic anomalies and lead–zinc deposits, we employed various potential field conversion techniques, including the reduction to the pole, vertical derivatives, upward continuation, and residual anomaly analysis techniques. Secondly, we investigated the metallogenic sites within this region and provided a comprehensive summary of the metallogenic circumstances and characteristics related to aeromagnetic prospecting. Thirdly, we employed human–computer interaction fitting inversion techniques to predict the potential for lead–zinc mine prospecting in areas exhibiting aeromagnetic anomalies. The study underscores the significance of high-amplitude and large-scale aeromagnetic anomalies in the study area. Furthermore, we examined the interplay between intrusive rocks, strata, and structural elements within the region to identify favorable conditions for lead–zinc mineralization. As a result of our analysis and discussions, a location was predicted where a lead–zinc mine may exist. The research methodology outlined in this article provides valuable insights for future lead–zinc mine exploration efforts in areas characterized by similar geological conditions.

Keywords: dynamic delta wing; high-precision aeromagnetic data; lead–zinc mine; aeromagnetic data inversion

Citation: Ji, N.; Qin, X.; Wu, H.; Wang, Z.; Du, W.; Liu, Y.; Zhang, T.; Zhang, S.; Shi, Q. Occurrence Characteristics of Lead–Zinc Mine and Low-Flying Aeromagnetic Prospecting in a Forested Region of Yichun City. *Minerals* **2023**, *13*, 1414. https://doi.org/10.3390/min13111414

Academic Editors: Shuang Liu, Lianghui Guo, Guoqing Ma and Emilio L. Pueyo

Received: 28 September 2023
Revised: 31 October 2023
Accepted: 2 November 2023
Published: 6 November 2023

1. Introduction

Magnetic prospecting is one of the key methods for mineral resources exploration, using the Earth's magnetic field to carry out subsurface surveys [1]. It is possible to acquire details about the magnetic properties and the geographical distribution of subsurface materials by measuring and analyzing the Earth's magnetic field anomalies. Magnetic prospecting has been widely applied in many distinct fields, such as the exploration of petroleum and mineral resources, the monitoring of environmental quality, and the

engineering of geological surveys [2]. Ground magnetic survey [3] and aeromagnetic survey are two typical types of magnetic surveys. For small-area, large-scale exploration activities, a traditional ground magnetic survey is appropriate. However, it may be labor-intensive, ineffective, and dangerous for the operators and equipment. The rugged terrain and other factors also create many exploring blind spots. The aeromagnetic survey [4–14] is a high technology that combines geophysical exploration techniques with aviation technology [15–18]. It is used to investigate and identify mineral resources and subsurface geological structures, with high-precision optically pumped magnetometers and real-time compensation systems mounted on the aircraft to detect changes in the magnetic field while the aircraft is in operation. An aeromagnetic survey has many advantages, including deeper exploration depths, lower cost, high efficiency, and practicability in large-scale operations. It is considered one of the symbols of the modernization of geological exploration [19]. However, the mainstream platforms used in aeromagnetic exploration, such as fixed-wing aircraft and helicopters, require relatively high flying altitudes and the use of suitable airports as bases. As a result, they have some limitations in large-scale measurements and are constrained by relatively short flight ranges [20–22]. Dynamic delta wing aeromagnetic platforms [23,24], which has evolved from outdoor sports, offers advantages such as flexibility, lightness, low flight speed, low flying altitude, ease of transportation, and convenient takeoff and landing. Besides, they are very economical, requiring minimal operating and maintenance expenses. In addition, large-scale operations in small and medium-sized areas also make them less dangerous for employees. Therefore, it makes up for the disadvantages of surface magnetic methods and other airborne magnetic survey platforms.

In order to perform high-precision magnetic surveys in the range from low-altitude (actual altitude 0–1000 m) to ultra-low-altitude (actual altitude 0–100 m), the low-altitude dynamic delta wing aeromagnetic survey system, with the integration of advanced software and hardware technologies, uses a powered dynamic delta wing as the flight carrier. The system consists of six parts including a powered delta wing, a navigation controller, a magnetic survey system, a magnetic compensation system, a positioning system, and a digital acquisition system (Figure 1). These six components are reorganized into three systems: the flight carrier system, the magnetic measurement system, and the data acquisition system.

Figure 1. The dynamic delta wing aeromagnetic survey system in a low-altitude range.

The 400 km range flight carrier system (Figure 1) is an aircraft, which can operate within a maximum radius of 50 km, utilized in regions where it is challenging for people to work and take up residence due to poor traffic conditions. It is not necessary to use standard airports or runways because the flight conditions are simple [25–30]; aside from the engine, the whole fuselage is primarily constructed of non-magnetic aviation aluminum

with fabric wings. With a width of 2.5 m and a length of less than 4.0 m, the overall mass of the aircraft is less than 300 kg. The glider's transport vehicle and hangar are made of a small van, making it easier to assemble, disassemble, and transfer during field flight operations (Figure 2). The magnetic measurement system comprises a helium magnetometer and a saturated three-component magnetometer. The sensitivity of the helium magnetometer (RS-GB10) is ±0.001 nT, with an accuracy of 0.01 nT, a sample rate of 0.5/s, and a range of 35,000 to 70,000 nT. The three-component automatic compensation device, which is also called saturated three-component magnetometer, measures the magnetic field. When the magnetic field sensor and the airplane are in different locations, the influence of the aircraft changes. There could be anomalies in a course when the compensation is insufficient, and there will be a systematic bias in the anomalies detected in different courses. The saturated three-component magnetometer's aim is to reduce such errors. The magnetic survey collector GB-10 is used in the data acquisition system. The system is used to set the flight survey lines before takeoff. The pilot will first navigate and locate, on the basis of a GPS, the pre-set flight survey lines and will fly while measuring and recording the flight route in real-time, depending on the navigation measurement data provided on the screen. All flight-related data can be immediately exported from the system after the flight.

(**a**) (**b**)

Figure 2. (**a**,**b**) The transport and storage of dynamic delta win.

The research area for this paper is located in a forested region of Yichun city, where there are well-developed intrusive rocks, notably monzonitic granite from the Late Triassic. These rocks are largely exposed, with an appearance of bedrocks and vein-like and lens-like rocks, and the trending direction of these rocks is mostly aligning with faults and fracture zones. The lithology is composed of monzonitic granite with fine to medium-sized grains, mylonitic granite with fine to medium-sized grains (biotite), and monzonitic granite with coarse to medium-sized grains. During the intrusion of magma, there existed contact metasomatism between the rocks of the Qianshan formation and intrusive rocks which have a close relationship with the mineralization of tin and copper. Intrusive rocks are also mineral-surrounding rocks, primarily found in silica–carbonate rocks and mineral-rich strata created by post-Late Triassic hydrothermal activity. The intrusive rocks formed at this stage are appropriate geological bodies for mineralization, especially for non-ferrous metals such as molybdenum, lead, and zinc [31].

The Xiaoxilin lead–zinc deposit founded in the Yichun region is a hydrothermal contact-metasomatic deposit. It is nestled within the contact zone between the upper Ordovician Qianshan formation's marble and the Late Triassic–Early Jurassic monzonitic granite. There are many types of alterations in the surrounding rocks, and silicification, thermalization, mangano-siderite, mineral-bearing dolomitization, garnet chlorination, skarn mineralization, sericitization, and biotitization are those related to mineralization. There are more than 30 distinct types of metals and gangue minerals that comprise ores, mainly including pyrrhotite, pyrite, sphalerite, galena, magnetite, dolomite, and calcite [32].

There were some anomalies of lead, zinc, and molybdenum in the monzonitic granite during the period from the Late Triassic to the Early Jurassic. The anomalies of lead and

zinc mainly occurred within the contact zone between the granite and the stratum, while the anomalies of molybdenum occurred within the granite.

Granites from this age are magma-mixed rocks, and the fine-grained porphyritic granites of the Early Cretaceous sporadically occur in the form of stocks in the study area, where there are also vein rocks. Therefore, these factors are likely to lead to the subsequent enrichment of elements such as lead, zinc, molybdenum, creating favorable conditions for mineralization. The Late Triassic–Early Jurassic monzonitic granite, a symbolic intrusive rock in this region, serves as a marker for mineral exploration. Therefore, it will be easy to explore the lead–zinc deposits in the study area.

The study area is a typical geological survey area where there are dense forests, shrubs, and a swamp, the depth of which is generally between 0 and 3 m, with some specific areas deeper than 3 m. Therefore, it is hard to carry out geophysical prospecting operations in such a place, with poor transportation and working conditions. The dynamic delta wing magnetic system, characterized by its efficiency, adaptability, and longer endurance, can efficiently reduce human disturbances and the disturbances brough about by anomalies caused by magnetic sources in shallow layers. As such, it is suitable for use in areas where rocks are mostly covered by forests, swamps, and slope deposits and where there are some human disturbances, meaning that surface geophysical explorations are hard to carry out. Therefore, this paper adopts the dynamic delta wing magnetic survey method to carry out the research for lead–zinc deposits in the study area.

2. Theory and Method

2.1. Method Principle

Polygonal section is a key method for analyzing gravity and magnetic data through human–computer interactions, as it has a high computing speed and can reasonably approximate the shape of any object. It can be used to resolve the forward and inversion problems of gravity and magnetic anomalies on the basis of exploration data. The polygonal section method can approximate any shape with an arbitrary precision, since the number of edges of a polygon can be arbitrary. In addition, each section's effect can be described with precise analytical expressions [31,32].

For the two-dimensional numerical model shown in Figure 3, κ is assumed to be the magnetic susceptibility; M_s is the surrounding geomagnetic field intensity; I_0 is the magnetization inclination; A' is the angle of the positive x direction to the magnetic north in a counterclockwise direction, and the direction of the measurement of the magnetic field is assumed to be consistent with that of the geomagnetic field. The formula for the Z_a and H_{ax} components of the two-dimensional numerical model are as follows:

$$\begin{cases} Z_a = \frac{\mu_0 M_s}{4\pi G\rho}(V_{xz}cosi_s + V_{zz}sini_s) \\ H_{ax} = \frac{\mu_0 M_s}{4\pi G\rho}(-V_{zz}cosi_s + V_{xz}sini_s) \end{cases}, \tag{1}$$

Among them, G is the constant of universal gravitation; μ_0 is the vacuum permeability; ρ is the density of the two-dimension numerical model; V_{xz} and V_{zz} are the gravitational potential along various coordinate axes; Z_a is the vertical component of the magnetic anomaly; H_{ax} is the horizontal component of the magnetic anomaly, and i_s is the effective magnetization inclination angle of M_s. From this, the components Z_a and H_{ax} and the overall magnetic anomaly ΔT can be deduced as follows:

$$\begin{cases} \Delta T = \frac{\mu_0}{4\pi}\frac{\kappa M_s}{G\rho}\left[\left(sinI_0\frac{\partial}{\partial z}V_z + cos_0IcosA'\frac{\partial}{\partial x}V_x\right)sinI_0 + \left(sinI_0\frac{\partial}{\partial z}V_x - cosI_0cosA'\frac{\partial}{\partial z}V_z\right)cosI_0cosA'\right] \\ \quad = Z_a sinI_0 + H_{ax}cosI_0cosA' \\ Z_a = \frac{\mu_0}{4\pi}\frac{\kappa M_s}{G\rho}\left(sinI_0\frac{\partial}{\partial z}V_z + cosI_0cosA'\frac{\partial}{\partial x}V_x\right) = \frac{\mu_0}{2\pi}\kappa M_s\left[sinI_0\sum_{n=1}^{N}\left(\frac{\partial}{\partial z}Z_n\right) + cosI_0cosA'\sum_{n=1}^{N}\left(\frac{\partial}{\partial z}X_n\right)\right] \\ H_{ax} = \frac{\mu_0}{4\pi}\frac{\kappa M_s}{G\rho}\left(sinI_0\frac{\partial}{\partial z}V_x - cosI_0cosA'\frac{\partial}{\partial z}V_z\right) = \frac{\mu_0}{2\pi}\kappa M_s\left[sinI_0\sum_{n=1}^{N}\left(\frac{\partial}{\partial z}X_n\right) - cosI_0cosA'\sum_{n=1}^{N}\left(\frac{\partial}{\partial z}Z_n\right)\right] \end{cases} \tag{2}$$

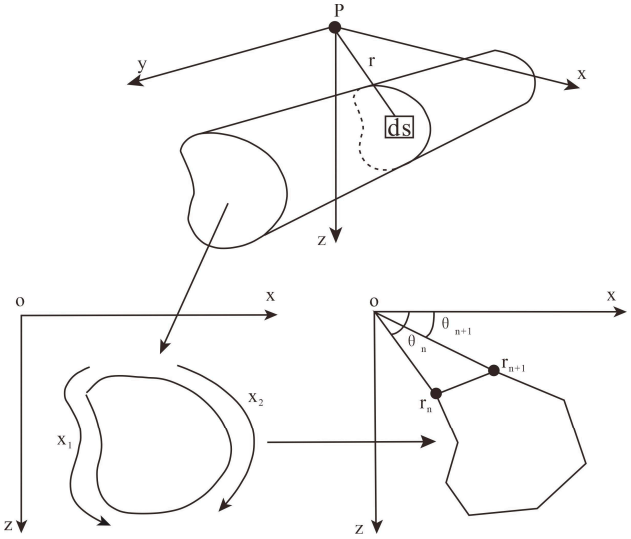

Figure 3. A polygon graph in two dimensions with any cross-section.

Here, ΔT is the total magnetic intensity; V_x and V_z are the respective partial differential of V in the x and z directions. In addition, $Z_n = A\left[(\theta_n - \theta_{n+1}) + Bln\frac{r_{n+1}}{r_n}\right]$ and $X_n = A\left[-(\theta_n - \theta_{n+1}) + Bln\frac{r_{n+1}}{r_n}\right]$ (Set to $x_i = x_i - x$ and $z_i = z_i - z$ ($i = n$ or $n+1$), respectively, so that the partial differential calculation can be carried out). Among this, $V_x = 2G\rho\sum_{n=1}^{N} X_n$ and $V_z = 2G\rho\sum_{n=1}^{N} Z_n$; z_n and z_{n+1} are the respective z coordinates of the two endpoints of the nth edge of the polygon; x_n and x_{n+1} are the z coordinates of the two endpoints of the nth edge of the polygon, respectively; A and B are the matrices of order $m \times n$; θ is the angle between the cross-sectional line segment and the coordinate axis; r is the distance between the observation point and the end or the center point of the field source. The calculating partial derivatives are as follows:

$$\begin{cases} \frac{\partial}{\partial z}Z_n = \frac{(x_{n+1}-x_n)^2}{R^2} - \left[(\theta_n - \theta_{n+1}) + \frac{z_{n+1}-z_n}{x_{n+1}-x_n} ln\frac{r_{n+1}}{r_n}\right] - P \\ \frac{\partial}{\partial x}Z_n = \frac{-(x_{n+1}-x_n)(x_{n+1}-z_n)}{R^2}\left[(\theta_n - \theta_{n+1})\frac{z_{n+1}-z_n}{x_{n+1}-x_n} ln\frac{r_{n+1}}{r_n}\right] + Q \\ \frac{\partial}{\partial z}X_n = -\frac{(x_{n+1}-x_n)^2}{R^2}\left[\frac{z_{n+1}-z_n}{x_{n+1}-x_n}(\theta_n - \theta_{n+1}) - ln\frac{r_{n+1}}{r_n}\right] + Q \\ \frac{\partial}{\partial x}X_n = \frac{(x_{n+1}-x_n)(z_{n+1}-z_n)}{R^2}\left[\frac{z_{n+1}-z_n}{x_{n+1}-x_n}(\theta_n - \theta_{n+1}) - ln\frac{r_{n+1}}{r_n}\right] + P \end{cases} \quad (3)$$

Then,

$$\begin{cases} R^2 = (x_{n+1} - x_n)^2 + (z_{n+1} - z_n)^2 \\ P = \frac{z_{n+1}\cdot x_n - x_{n+1}\cdot z_n}{R^2}\left[\frac{x_n(x_{n+1}-x_n)-z_n(z_{n+1}-z_n)}{r_n^2} - \frac{x_{n+1}(x_{n+1}-x_n)-z_{n+1}(z_{n+1}-z_n)}{r_{n+1}^2}\right] \\ Q = \frac{z_{n+1}\cdot x_n - x_{n+1}\cdot z_n}{R^2}\left[\frac{x_n(z_{n+1}-z_n)-z_n(x_{n+1}-x_n)}{r_n^2} - \frac{x_{n+1}(z_{n+1}-z_n)-z_{n+1}(x_{n+1}-x_n)}{r_{n+1}^2}\right] \end{cases} \quad (4)$$

The magnetic anomaly of any combination of several two-dimensional models can be calculated using the equation above.

2.2. Magnetic Data Fitting in 2.5D with Human–Computer Interaction

Magnetic profile joint inversion is used to estimate the depth and the geometrical characteristics of a geological interface based on graphic geological profiles and data on rock magnetism. The initial model derives from a priori information on geophysics and geology. The model is continuously adjusted to make calculated values match the measured values closely,, enabling the intuitive forward and inverse modeling of magnetic profiles. Compared to the automated direct inversion techniques, the 2.5D human–computer inter-

active magnetic data inversion method is appropriate for inverting geological boundaries with significant differences in their physical characteristics, such as formation boundaries, intrusive bodies, folds, and faults. A 2.5D model in magnetic data refers to a geological mass that extends to a specific distance in the strike direction, with an arbitrarily shaped cross-section. Polygons can be used to simulate the shape of the cross-section. The model's magnetic anomaly value at any location in space can be determined as long as the vertex coordinates, orientation, length, and magnetization of the polygon are known. By comparing the calculated magnetic anomaly effect of the initial model with the measured magnetic anomaly along the profile, the model can be continuously adjusted until the difference between the calculated magnetic anomaly and the measured magnetic anomaly on the profile meets the predetermined accuracy (Figure 4).

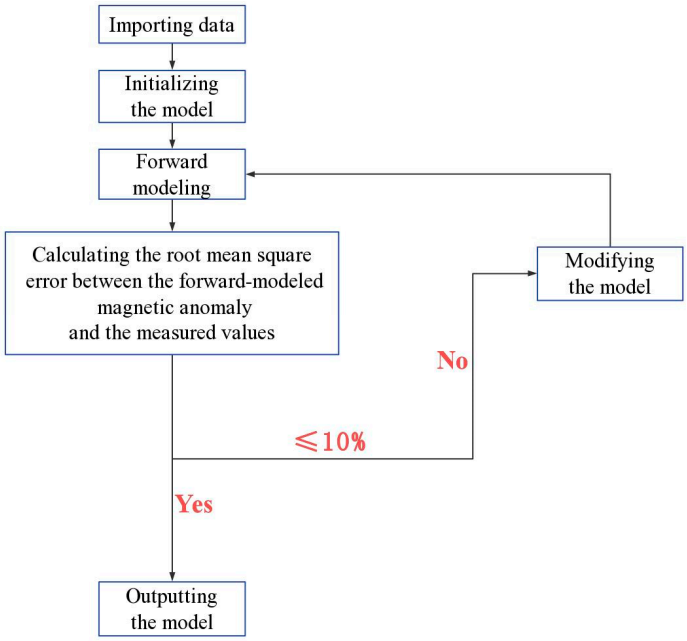

Figure 4. Diagram of the procedure for fitting human–computer interaction.

This 2.5-dimensional inversion utilizes the Oasis Montaj software, of which the GM-SYS profile simulation module is a user-friendly, feature-rich, and interactive heavy magnetic simulation software which can quickly build a geological model and test its accuracy by comparing the error between the model's heavy magnetic response and the collected data to create a model swiftly.

The specific steps are as follows:

(1) Import the measured magnetic anomaly data of the profile;
(2) Import the initial model and initial physical parameters;
(3) Add, delete, and modify the field source model based on the comparison between the theoretical anomalies of the module's forwarding and the measured anomalies;
(4) Continue until the root-mean-square (RMS) error between the theoretical anomalies of the forwarding and the measured anomalies is less than or equal to 10%;
(5) Output the inverse model [33–37].

3. Introduction to the Research Area

3.1. Location of the Study Area

The study area is one of the administrative districts in Yichun city, which is located in the northeast of the Heilongjiang province. It spans a total area of around 104.83 km^2. The geotectonic location is in the tertiary structural unit of the Yichun–Yanshou fold orogenic belt, an overlapped area between the Mongolian–Okhotsk collision orogenic belt and the outer margin of the Circum–Pacific subduction zones. The secondary tectonic belt is the

quaternary structural unit of the Wuxingzhen–Xilin composite-fold belt, which mainly comprises the lower Heilonggong formation of the Devonian and the Xilin group of the lower Cambrian [38,39].

3.2. Geology of the Study Area

3.2.1. Geological Structure

The fold structure of the Heilongjiang province can be roughly divided from east to west into three composite fold belts, i.e., the Fengmao–Chenming fold belt, the Wuxingzhen–Xilin fold belt, and the Cuiluan–Tieli fold belt. The fault structures in the Heilongjiang province are highly developed and are characterized by various scales and directions. There are two regional faults, as follows: the Xunke–Tieli–Shangzhi north–south lithosphere fault, which is more than 5000 km long and is located in the western part of the study area, and the Mudanjiang north–south lithosphere fault, which is longer than 5000 km but is located in the eastern part of the study area. In general, faults can be categorized according to their directions, such as nearly north–south trending faults, east–west trending faults, north–east trending faults, and north–west trending faults. According to a regional geological survey, the fold structure and the fault structure are the primary structural manifestations in the study area. The study area is located in the northern part of the Yichun–Yanshou polymetallic metallogenic belt (Figure 5), which belongs to the peripheral extension area of the Wuxing lead–zinc mine and the Wuxing iron–polymetallic mine. The tectonic position of the study area belongs to the Wuxing–Guansongzhen uplift zone in the middle of the Yichun–Yanshou fold orogenic belt, which is the overlapping area between the Mongolian–Okhotsk collision orogenic belt and the outer margin belt of the Circum–Pacific subduction belt. The Yichun–Yanshou belt is distributed in a north–south direction, with an extensive distribution range, adjacent to the Jiamusi block [40]. To the west of it is the Xunke–Tieli–Shangzhi fault, and to the east is the Jiayin–Yilan–Mudanjiang fault. The low-flying aeromagnetic study area is situated in the Wuxingzhen–Xilin complex's fold belt, which is a part of the Yichun–Yanshou polymetallic metallogenic belt.

3.2.2. Stratum

In the Yichun area, the geological strata become younger and younger from north to south and from east to west. The remnants of the strata from the Paleozoic, pre-Paleozoic, and Proterozoic eras are sporadically distributed within the granite formations. And, most of the rocks in these layers are metamorphic rocks. The strata from the Mesozoic and the later eras are broader and more developed [41].

Figure 6 is the regional geological map of the study area. The main strata in the study area are as follows: the lower Cambrian Qianshan formation ($\in_1 q$), the lithology of which is primarily composed of microcrystalline limestone, muddy limestone, marble, metamorphic siltstone, etc.; the Cambrian Laodaomiaogou formation ($\in_1 l$), the lithology of which is mainly composed of marl limestone, marble, metasandstone, and argillaceous slate; the Banzifang formation (K_1b), which comprises sedimentary rocks from continental volcanic eruptions; and the Honglin formation (Pt_1hn). Generally, there are monzogranite (medium-grained) ($T_3\eta\gamma$), granite ($O_2\gamma$), and granodiorite ($O_2\gamma\delta$) exposures in the research area. And, the Yanshanian diorite mass ($K_1\delta$) can be seen in the northeastern part of this area. The diorite mass is the cause of the anomaly in this area, and the anomaly's edge is located in the contact zone between the diorite mass and the sedimentary Laodaomiaogou formation ($\in_1 l$). In the anomaly area, nearly south–north linear structures exist. This demonstrates that a geological body can be affected by hydrothermal activities in a later period [42].

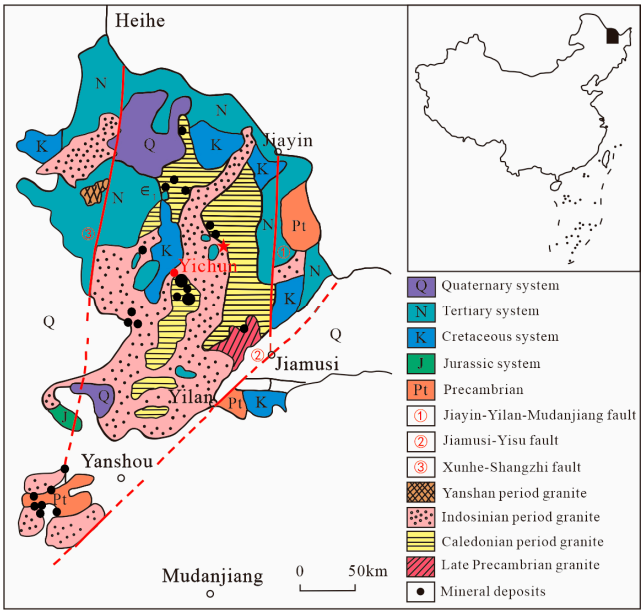

Figure 5. The approximate location of the research area and the geotectonic location of the Yichun area.

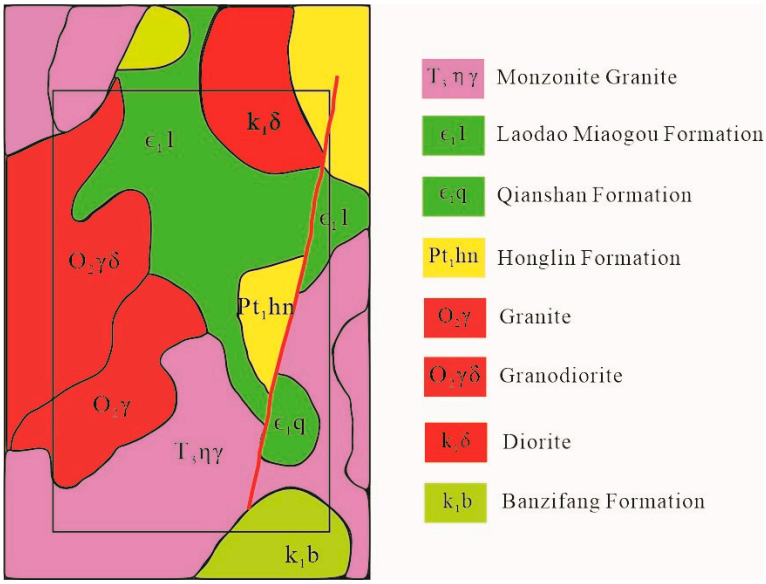

Figure 6. Regional geological map of the study area.

3.2.3. Intrusive Rock

Intrusive rocks are relatively well-developed in the study area, where they are primarily made up of Late Triassic monzogranite, widely exposed in the appearance of batholiths. The lithology of these intrusive rocks consists of mylonitized fine–medium-grained (biotite) monzogranite, mylonitized coarse–medium-grained (biotite) monzogranite, and fine–medium-grained (biotite) monzogranite. During magmatic intrusion, there was contact metasomatism between the intrusive rocks and the rocks of the Qianshan formation, and this is closely related to the mineralization of tin and copper. These intrusive rocks are also ore-forming, surrounding rocks, which are usually found in the skarn and ore-rich layers formed by hydrothermal fluids in the later period of the Late Triassic.

The regional features of a magnetic field are intimately connected to those of the geological units, which means that the magnetic field of Mesozoic basic–mesobasic volcanic rocks changes greatly, while the magnetic properties of Paleozoic metamorphic rocks are rather weak. It is challenging to categorize these magnetic fields as there are few differences

between intrusive rocks from different ages. As a sign of hydrothermal activity, vein rocks also serve as a source of material for the enrichment of ore-forming components [43].

4. Application

The Yichun area in the Heilongjiang province, situated in the Xiaoxing'anling metallogenic belt, is an important base for the metal–mineral sector and a large-scale metallogenic concentration of precious metals and non-ferrous metals in northern China. At present, the Yichun area has more than ten lead and zinc polymetallic deposits of various scales [44]. There are various types of minerals, such as Au, Ag, Cu, Pb, Zn, W, Sn, Mo, Fe, Ni, etc., all of which are urgently needed for economic development. In recent years, new deposits have been continuously discovered, and some progress has been made in mineral exploration. However, due to some objective restraints, such as the unique metallogenic geological background, complex metallogenic geological conditions, multiple metallogenic ages, thick vegetation on the surface, and poor transportation, the area has a relatively low level of basic geological research, and a series of fundamental geological issues, such resource prospect appraisal, have yet to be well resolved. Therefore, the search for new deposits is seriously affected, to some extent. This paper is going to carry out a preliminary prediction and analysis of the distribution of lead–zinc mines in the research region by applying the dynamic delta wing low-altitude magnetic survey technology [43].

4.1. Magnetic Petrophysics

Magnetic susceptibility and natural remanent magnetization (NRM) data related to magnetic field interpretation play a crucial role in geophysical research. They are among the key components that are based on aeromagnetic data, and, in order to gain a deeper understanding of subsurface geological structures and resource potential, geophysicists often utilize these data for three-dimensional geological modeling [45]. Rocks' magnetic susceptibility reflects their response to external magnetic fields, while the NRM represents the magnetic history recorded within rocks during their formation. Together, they influence magnetic anomalies' characteristics in aeromagnetic data.

These physical data not only play a critical role in geological interpretation but also are of paramount importance in forward-modeling calculations. Forward modeling is a numerical method used to simulate the response of underground rocks and mineral deposits to the Earth's magnetic field, aiding researchers in understanding how various geological and mineral structures impact the behavior of the magnetic field. Hence, the accuracy and comprehensive analysis of these data are vital for geological exploration and resource assessment.

The data in Table 1 are sourced from reference [46]. The measurements in this study were conducted using the Czech-manufactured KT-6 handheld magnetic susceptibility meter, which is known for its strong stability, ease of use, and ability to yield reliable magnetic susceptibility data. The measurement work described in the reference above primarily relied on geological maps and topographic maps, with a focus on in situ measurements at rock outcrops. Fresh rock surfaces at rock outcrops were chosen, and, for each physical property point, no fewer than 30 data points were collected within a 10-m radius (of the same rock type). This approach accounted for rocks (minerals) of different ages, different lithologies, and various geological regions, ensuring a relatively uniform spatial distribution. In this study, a total of 3236 physical property points were measured, resulting in 96,930 valid magnetic susceptibility data points. Additionally, 971 oriented samples were collected and measured.

Table 1. Magnetic susceptibility and natural remanent magnetization of volcanic rocks.

Chronostratigraphic Unit	Rock Type	Susceptibility (10^{-6} SI)			Natural Remanent Magnetization (10^{-3} A/m)	
		Samples	Range of Variation	Average	Samples	Range of Variation
Quaternary	Stomatal basalt, almond-shaped olivine basalt, olivine basalt, basalt	2102	30–26,620	4210	56	687–22,865
Cretaceous	Pyroxene andesite, pyroxene andesite porphyrite, andesite basalt, olivine basalt	3780	6420–33,300	18,070	151	82–5970
	Andesite porphyrite, andesite, andesitic tuff, breccia tuff	3900	410–18,400	6770	244	45–6451
	Tuff, tuff lava, perlite	1620	10–8670	1890	128	59–2757
	Dacite, rhyolite, rhyolite porphyry, conglomerate tuff, gravelly tuff, tuffaceous lava	606	10–4830	180		
Jurassic	Tuff, tuffaceous-fused breccia	270	3560–23,700	12,100		
	Rhyolite porphyry tuff lava, tuff lava, tuff sandstone	2172	10–13,300	4210	33	80–469
	Rhyolite porphyry	275	70–1480	330		
Triassic	Andesite	42	510–13,690	5830		
Triassic-Permian	Andesitic tuff, tuff lava	1170	10–29,800	6050	11	79–453
	Rhyolite porphyry, tuff	690	10–10,600	2970		
Permian-Carboniferous	Tuff, andesitic tuff	241	130–9900	1550		
Ordovician	Gray-green tuff lava	91	190–26,690	13,870		
Cambrian	Rhyolite porphyry tuff lava	180	3100–17,900	10,000	31	47–214

The volcanic rocks in the study area generally formed before the Mesozoic era, encompassing a range from acidic to basic compositions. Overall, they exhibit dramatic variations in their magnetic susceptibility, characterized by a dispersed distribution and a tendency for the magnetic susceptibility to increase from the acidic to the basic compositions. As observed in Table 1, the magnetic susceptibility of the Quaternary rocks in the area exhibits the greatest variability, spanning a range of $(30 \text{ to } 26,620) \times 10^{-6}$ SI, with a high remanent magnetization of $22,865 \times 10^{-3}$ A/m. These rocks are a primary contributor to the disturbed magnetic field within the formation area. Cretaceous volcanic rocks are also prevalent in the region, typically having a magnetic susceptibility around 18,070 $\times 10^{-6}$ SI, with variations of (6420 and 33,300) $\times 10^{-6}$ SI. Their remanent magnetization can reach a value as high as 5970 $\times 10^{-3}$ A/m, often resulting in a highly variable magnetic field pattern. Acidic volcanic rocks such as rhyolites, andesites, and dacites exhibit relatively weaker magnetic properties, with a susceptibility range of (10 to 4830) $\times 10^{-6}$ SI.

From Table 2 (where rock types with similar magnetic susceptibility from the same geological era have been merged), it is evident that, in the study area, the Proterozoic dolerites exhibit the strongest magnetism, with magnetic susceptibilities ranges of (21,530 to 185,000) $\times 10^{-6}$ SI, typically around 52,190 $\times 10^{-6}$ SI, and a high remanent magnetization of 8441 $\times 10^{-3}$ A/m. Acidic intrusive rocks from the Mesozoic and Paleozoic eras are

widespread and generally exhibit moderately low magnetism. The weakest magnetism is observed in Mesozoic syenite porphyry, Late Paleozoic granite, and some acidic dikes. Overall, as the lithology of the rocks changes from acidic to ultrabasic, their magnetic susceptibility gradually increases. This is related to the higher concentration of ferromagnetic minerals in the rocks, indicating that the primary factor influencing the magnetism of intrusive rocks is the composition of the original magma.

Table 2. Magnetic susceptibility and natural remanent magnetization of intrusive rocks.

Age	Rock Type	Susceptibility (10^{-6} SI)			Natural Remanent Magnetization (10^{-3} A/m)	
		Samples	Range of Variation	Average	Samples	Range of Variation
Mesozoic	Albitophyre	150	40–100	60		
	Alaskite granite, Syenogranite	5760	20–7110	2270		
	Biotite granite, Plagiogranite, Granite, Alkali feldspar granite, Granite porphyry	30,420	430–25,300	2860	216	38–584
	Diorite, Pyroxene diorite, Granodiorite	5820	320–49,100	12,390	147	229–5200
Late Paleozoic	Biotite granite, Plagiogranite, Monzogranite, Alkali feldspar granite	8580	10–7450	270		
	Alaskite granite, Porphyritic granodiorite	3240	20–7050	2120		
	Granodiorite	3450	340–30,000	8580		
Early Paleozoic	Mixed granite, Porphyritic granite	600	20–220	90		
	Cataclastic granite, Syenite granite, Biotite granite, Plagiogranite	3420	10–7660	710	55	0–65
	Granodiorite	120	650–7520	2840	14	32–196
	Diorite	150	400–14,700	6750		
	Gabbro	330	1280–45,900	15,820		
Mesoproterozoic	Mixed granite	300	100–1330	750		
	Peridotite	60	21530–185,000	52,190	11	3320–8441
Paleoproterozoic	Mixed rock, Mixed granite, Porphyritic mixed granite, Biotite granite	930	10–670	190		
	Biotite monzogranite	60	930–4530	2610		

From Table 3, it can be observed that the magnetic susceptibility of the magnetite ore in the Yichun area generally falls around 700,000 $\times 10^{-6}$ SI, with the maximum reaching up to 5,947,450 $\times 10^{-6}$ SI. The ore's remanent magnetization range of (91,600 to 681,400) $\times 10^{-3}$ A/m indicates an extremely strong magnetism. The measured siliciclastic rocks exhibit a moderate magnetism, with a magnetic susceptibility not exceeding 8000 $\times 10^{-6}$ SI. The siliciclastic rocks transformed from limestone have a magnetic susceptibility of no more than 2000 $\times 10^{-6}$ SI.

Table 3. Magnetic parameters of ore and surrounding rocks.

Ores and Surrounding Rocks	Samples	Susceptibility (10^{-6} SI)		Natural Remanent Magnetization (10^{-3} A/m)	
		Range of Variation	Average	Range of Variation	Average
Skarn	3	100–7750	2430		
Skarnization marble	1	20–1720	300		
Magnetized hornblende gabbro	21	36,820–23,2420	149,850		
Magnetite	11	164,010–5,947,450	701,830	91,600–681,400	255,000

The study area is characterized by an extensive distribution of intrusive rocks, predominantly acidic to intermediate-acidic in composition. Based on the magnetic properties and the combination of anomalies associated with different intrusive rocks, it is possible to delineate these intrusions. The magnetic field characteristics reflected in aeromagnetic measurements have a certain depth, and the differences in magnetic properties between the rock body, overlying strata, and surrounding rocks can effectively aid in identifying the lithology of concealed rock bodies and delineating their boundaries.

4.2. Data Acquisition

The low-flying aeromagnetic working area is situated in the Wuxingzhen–Xilin complex fold belt, a part of the Yichun–Yanshou polymetallic metallogenic belt. The magnetic field characteristics of this area are strongly tied to those of the geological units, characterized by substantial variations in the magnetic field of the Mesozoic basic–mesobasic volcanic rocks and the weak magnetic properties of the Paleozoic metamorphic rocks. It is challenging to categorize magnetic fields since there are not many differences between intrusive rocks from various ages. Granodiorite and alkali feldspar granite are among the rocks with a high magnetic field, while metamorphic siltstone is among those with a low magnetic field. In addition, there are interfering magnetic anomalies caused by diorite porphyrite veins and magnetic anomalies caused by magnetite [47].

We used the aeromagnetic exploration instrument introduced in the Section 1 of this paper to acquire the magnetic anomalies in the study area. For this measurement, the scale was set to 1:10,000, the line spacing was 100 m, and the measurement lines were oriented at 90° (east–west) based on the geological data and previous aeromagnetic data. The total number of measurement points amounted to approximately 500,000 physical data points. The surveyed area covered 104.83 km^2, with a control area spanning 121.44 km^2, as depicted in Figure 7a.

4.3. Data Processing

The magnetic anomalies in the study area vary in form and in amplitude (Figure 7a). The main positive and negative ΔT anomalies are relatively concentrated.

The distribution of the ΔT magnetic anomalies in the study area is relatively regular. The maximum value of the measured ΔT magnetic anomaly is 775 nT, and the minimum value is −239 nT. The anomalies in general exhibit a north-northeastern (NNE) orientation. The general morphology of the magnetic anomalies is planar and linear, and it can be divided into the following three categories: high-value positive planar anomalies in the north, low and mild linear anomalies in the middle, and negative anomalies in the south.

The magnetic field's strength in the study area is 55,753.3 nT, with a magnetic inclination angle of 65°13′ and a magnetic declination angle of −11°45′. The main features after the RTP are an increase in the strength of the positive anomalies, a northward movement of the anomaly peak, and an improved regularity in the anomaly's arrangement. In the eastern part of the study area, the fine anomalies are basically connected. The morphology of the local anomalies also varies, but these changes follow different rules, and some anomalies

tend to stretch in the north–south direction. The anomaly variations in this area are mainly in the north–south direction and very few in the east–west direction (Figure 7b). In the northeastern corner of the study area, there is an increase in the amplitude of the large-scale positive anomalies, and the boundaries become more transparent. The magnetic anomalies after the RTP can better manifest the characteristics of the geological structures.

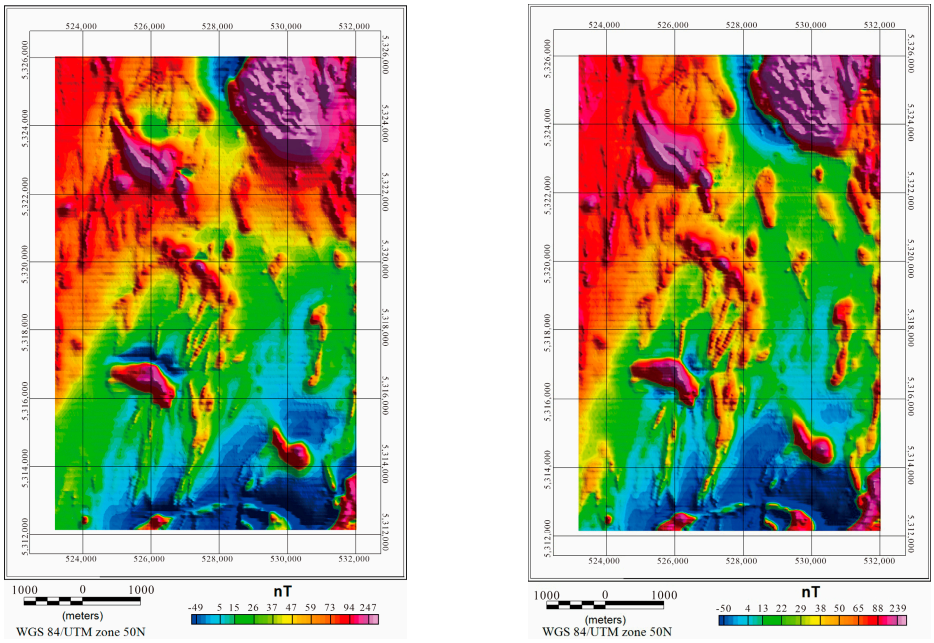

Figure 7. Aeromagnetic ΔT processing effect comparison. (**a**) Aeromagnetic ΔT anomaly and (**b**) aeromagnetic ΔT after reduction to the pole of magnetic field (RTP).

To eliminate a shallow magnetic interference, information deep below the surface is extracted using the upward continuation in the frequency domain, based on aeromagnetic ΔT grid data after RTP. After performing an upward continuation of 500 m to ΔT anomalies, all the ΔT anomalies on the observing plane in the study area vanished. The zonation of the positive anomalies in the north, of the low and mild anomalies in the middle, and of the negative anomalies in the south became clearer, while the widespread and high-amplitude planar body mostly remained unaltered (Figure 8). This qualitatively reflects the fact that the anomaly source in the study area is deeply buried.

Figure 9 illustrates that the distribution of the geomagnetic anomalies in the study area is complicated, so large amounts of rock masses with high magnetic properties can be found in this area. Comparing Figures 7b and 8 shows that the geomagnetic anomalies in the study area are primarily impacted by deep geological bodies. Figure 9 serves as a critical point for determining rock masses (veins) and linear structures, since it not only highlights local anomalies, but also the fact that the location of these local anomalies is basically consistent with that of the magnetic bodies.

After extracting the residual anomalies in the study area, the local anomalies caused by small-scale shallow magnetic bodies were highlighted (Figure 10).

4.4. Anomaly Extraction

4.4.1. Inference of Anomaly

Based on the data processing results presented above and considering the geological context, it is inferred that the study area exhibits seven distinct high magnetic anomalies, as shown in Figure 11. These seven anomalies will be analyzed in the following sections.

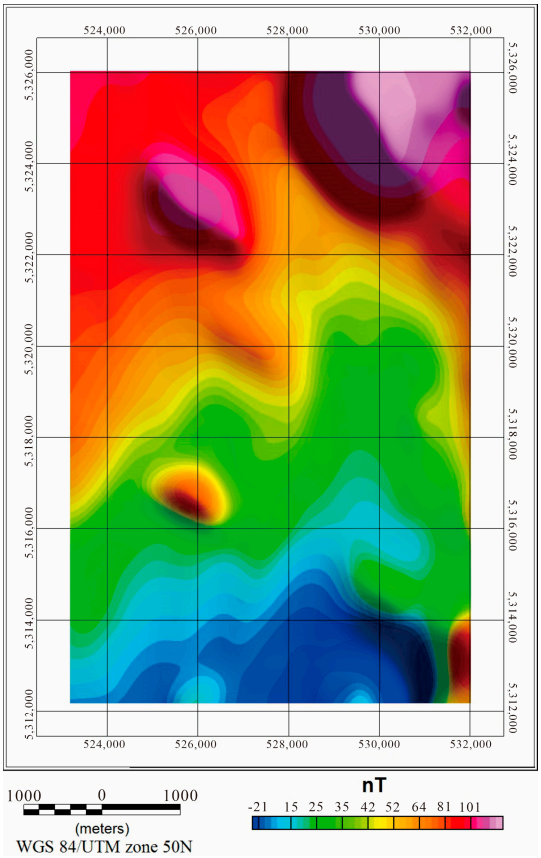

Figure 8. Aeromagnetic ΔT processing diagram for upward continuation of 500 m after RTP.

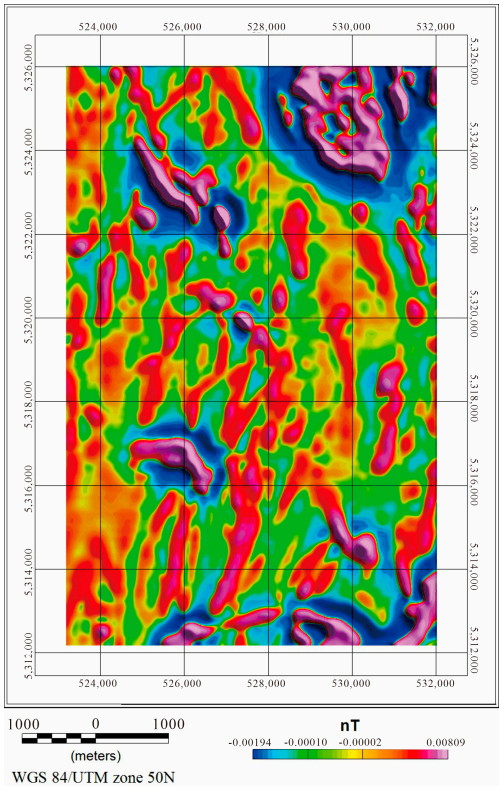

Figure 9. Aeromagnetic ΔT upward continuation of 200 m and vertical second derivative after RTP.

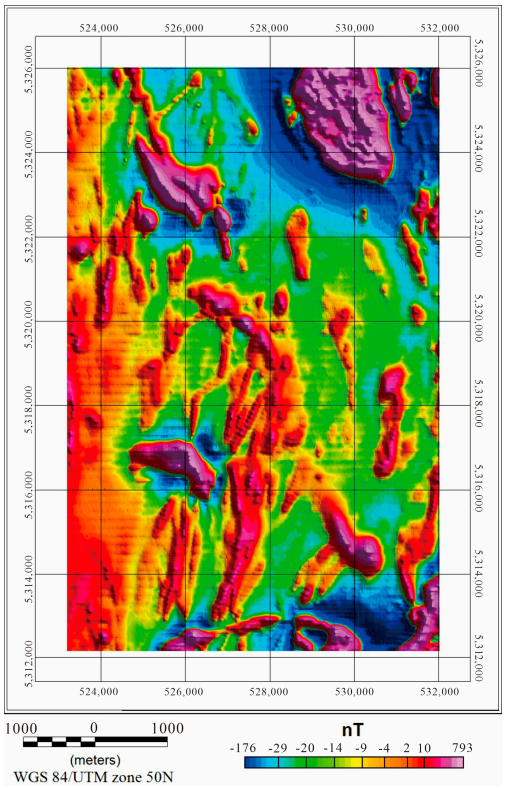

Figure 10. Aeromagnetic ΔT residual anomalies extraction processing diagram after RTP.

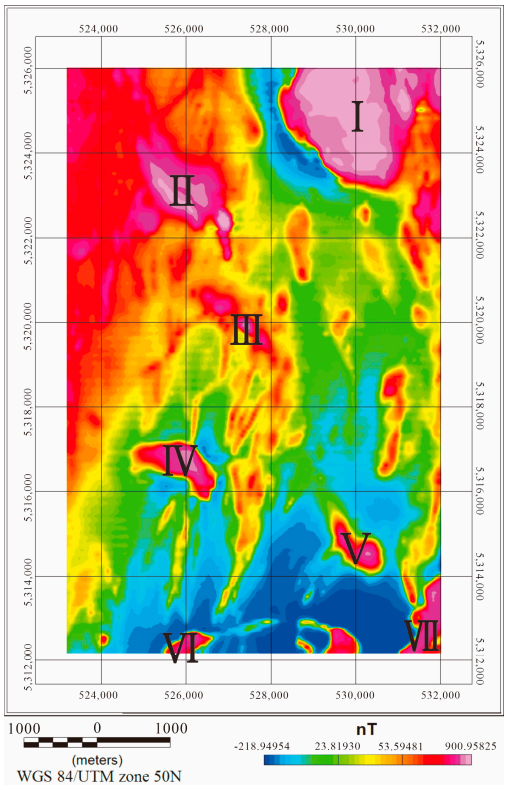

Figure 11. The division of anomalies and their numbering.

- I anomaly

The I anomaly, located in the northeast part of the study area, extends in the north–south direction with a vast size, appearing as a plane, the north side of which remains open.

The I anomaly extends 3.2 km in a northwest-southeast direction, with a width of 2 km, covering an area of 10.6 km^2. The anomaly's intensity is 120–700 nT. The corresponding surface geology is the Yanshanian diorite rock mass ($K_1\delta$), and the anomaly's edge is located within the contact zone between the diorite rock mass and the sedimentary strata of the Laodaomiaogou formation ($\in_1 l$). The anomaly is caused by the diorite rock mass, and nearly north–south linear structures are developed in the anomaly area. Given the absence of any diorite-related ore deposits and occurrences in the area, this anomaly lacks the potential for deposits' discovery.

- II Anomaly

The II anomaly is located in the southwest part of the I anomaly, appearing as an elongate shape in the northwest direction. With an area of 0.7 km^2, it is 1.2 km long in a northwest-southeast direction, with a width of about 0.6 km. The anomaly's intensity is 100–780 nT. According to the data processing results, the feature of the II anomaly after the RTP is similar to that of the I anomaly. It can be speculated that the II anomaly may be caused by diorite veins. The anomaly's edge is located within the contact zone between the Laodaomiaogou formation ($\in_1 l$) and the rock mass. The II anomaly has no prospecting potential.

- III Anomaly

The III anomaly is located on the south side of the II anomaly, in the middle of the study area. It extends in the shape of a strip in the north-west direction, with a length of 3.4 km and a width of 1.3 km, covering an area of about 2.8 km^2. The anomaly's intensity is 20–134 nT. According to the results of the data processing, the III anomaly after the RTP is located within the contact zone between the surface geological Ordovician granite and the Laodaomiaogou formation ($\in_1 l$), and it can be speculated that the anomaly is caused by the contact metasomatism between the granite rock mass and the formation. The III anomaly is located in multiple areas, characterized by a nearly north-south linear structure, and lacks mineralization potential, requiring further investigation.

- IV Anomaly

The IV anomaly is located on the south side of III anomaly and in the southern part of the study area. The morphology of the IV anomaly is approximately regular and intact, remaining closed in general. The anomaly extends by 2.5 km in length in the east–west direction, with a width of about 1.7 km, covering an area of 4 km^2. The anomaly's intensity ranges from -53 to 265 nT. The location and shape of the IV anomaly after the RTP correspond to those of the surface geological Andesan dikes. The anomaly is generally located in the exposed area of the Late Triassic–Early Jurassic monzogranite. The magnetic susceptibility of the Indosinian Yanshan monzonitic granite ranges from 50 to 150 $\times$ $10^{-6}4\pi$ SI, while the magnetic susceptibility of the andesite is around 1500 $\times$ $10^{-6}4\pi$ SI. It can be speculated that the anomaly is caused by intrusive andesite or andesite porphyrite veins. The overall anomaly is located in the intersection of multiple nearly north–south linear structural anomalies. The prospect for mineral prospecting is not optimistic and further work will be needed.

- V Anomaly

The V anomaly is located in the southeastern part of the study area. It is an ellipse with its axis stretching in the north-west direction and is enclosed in general. It measures 2.5 km along the axis and is roughly 1.5 km wide, covering an area of 2.8 km^2. The anomaly's intensity varies from -33 nT to 237 nT. The surface geology of the V anomaly can be found within the contact zone between the Cambrian Qianshan formation ($\in_1 q$) and the Late Triassic–Early Jurassic monzogranite, where granite porphyry veins and fine-grained veins also exist. The Late Triassic–Early Jurassic monzogranite is a notable intrusive rock for mineral exploration in the study area, and it is abundantly exposed. This phase of intrusive rocks, primarily consisting of hydrothermal metasomatic molybdenum

tin and lead–zinc deposits, is intimately associated with mineralization and is a favored ore-forming geological body in this area.

The entire anomaly area is traversed by the NNE trending fault. In the northern part of the V anomaly lies a limestone mine, in the Quanhe Forest Farm, where limestone from the Qianshan formation can be explored. According to the magnetic features and the surface geology of this anomaly, it can be deduced that this anomaly formed as a result of the contact metasomatism within the contact zone between the Cambrian Qianshan formation and the Late Triassic–Early Jurassic monzogranite and that it is closely related to the mineralization of tin and copper. The main anomaly is thought to have been caused by skarn and hydrothermal filling and metasomatism, and the intrusive rocks in this area are also ore-forming, surrounding rocks. The V anomaly, related to ore-controlling factors, is closely associated with mineralization.

- VI Anomaly

The VI anomaly is located in the southern edge of the study area and remains unenclosed. It appears as an oval plane, with its axis in the east-north direction. The anomaly is about 1.8 km long along the axis and about 0.85 km wide, covering an area of 1.2 km^2. The anomaly's intensity varies from −111 to 139 nT. The surface geology of the anomaly corresponds to that of the area where the granite fine-grained rock veins occur. It can be speculated that the VI anomaly is caused by these veins. The prospecting prospect in this area is not optimistic, and more work is required.

- VII Anomaly

The VII anomaly, which is unenclosed, is located in the southeastern edge of the study area, covering an area of about 3.8 km^2. The anomaly's intensity ranges from −230 to 181 nT. The surface geology of the VII anomaly consists of the middle Ordovician monzonitic granite and andesite and of the andesite veins of the Lower Cretaceous Banzifang formation. The magnetic susceptibility of the andesite is high. The anomaly is thought to have been caused by andesite minerals, and there is little hope of being able to prospect in this anomaly area.

4.4.2. Inference of Rock Mass Distribution

According to the morphology of the magnetic anomaly after RTP and by identifying boundaries through analytic signal amplitude(ASA)s, six distributions of rock mass (vein) within the area have been determined, which are consistent with the anomaly's distribution. As shown in Figure 12, the bottom image is the amplitude of the analytic signal's diagram. The largest rock mass is found in the northeastern part of the study area, in an oval shape, while other lenticular anomalies of various sizes are distributed in the middle and western regions of the study area. The rock mass V is speculated to be monzogranite.

4.4.3. Linear Structural Distribution

The magnetic field's features of this area are strongly related to the geological units', characterized by substantial variations in the magnetic field of the Mesozoic basic–mesobasic volcanic rocks and the relatively weak magnetic properties of the Paleozoic metamorphic rocks (Figure 13). The magnetic basement in the study area is deep in the north and shallow in the south, with noticeable gradient changes.

This report splits the fault structures in the study area according to the results of the aeromagnetic survey and estimates the distribution of the ten lines (or structures) in the study area (Figure 12). The linear faults in the study area are clearly developed on a large scale and in a complete morphology, extending in an NNE orientation. The area is believed to be strongly associated with the magmatic activity of the Caledonian and Indosinian periods and can be a favorable foundation for lead–zinc mineralization [48].

Comprehensive inferences have been produced in this study by thoroughly investigating the geological backgrounds in the study area, including the lithology, rock mass distribution, and fault structures (Figure 14). The V anomaly is considered to be related

to ore-controlling factors and has the necessary conditions for the formation of lead–zinc deposits. Therefore, we will now cut and process the AB profile traversing the V anomaly, as it is shown in Figure 14.

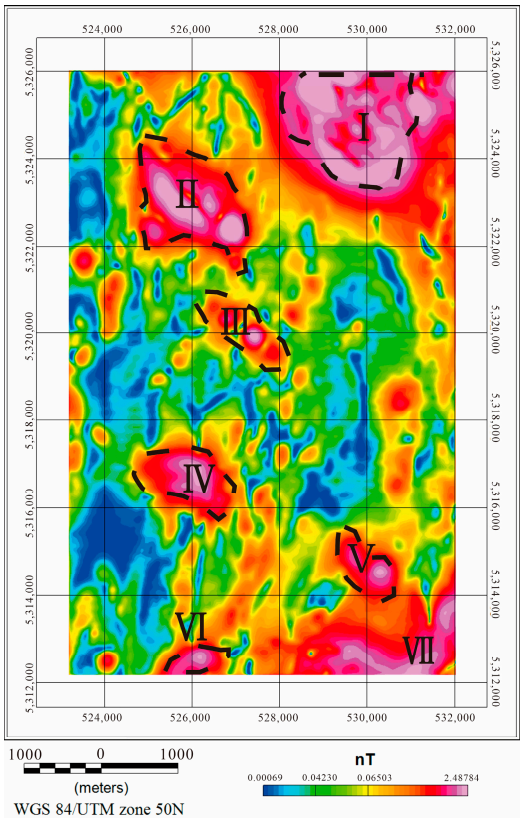

Figure 12. Inference map of rock mass (vein).

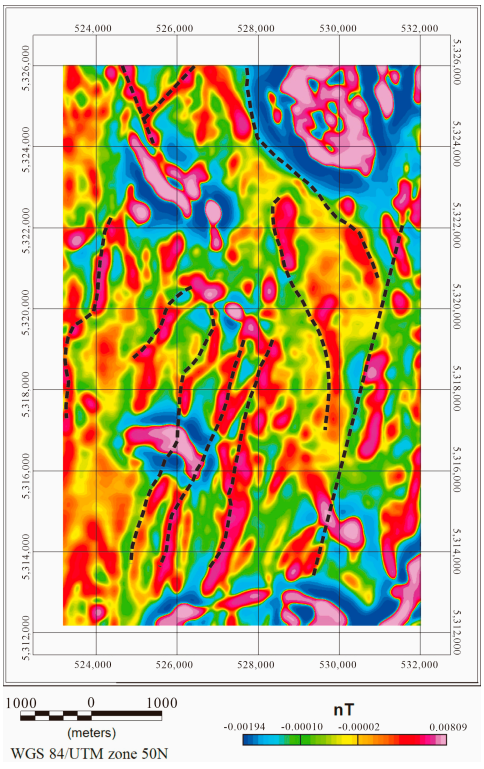

Figure 13. Linear structure inference graph.

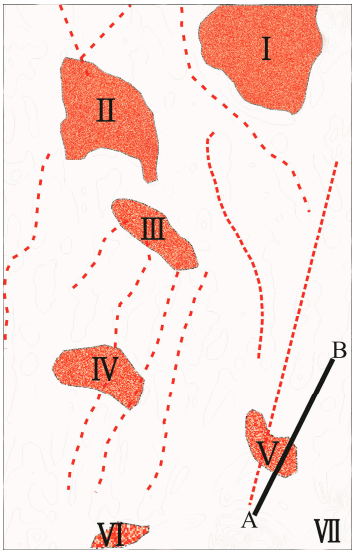

Figure 14. Comprehensive map of inferences.

4.5. Inversion and Interpretation

4.5.1. The Profile of V Anomaly

The profile of the V anomaly is hereby intercepted from south to north. Figure 15 shows the magnetic anomaly's morphology, which is low in the south and high in the north, progressively rising in the south and stabilizing in the north, with a clear anomaly uplift moving towards the north. The values of the magnetic anomalies in the profile approximately range from −110 to 190 nT.

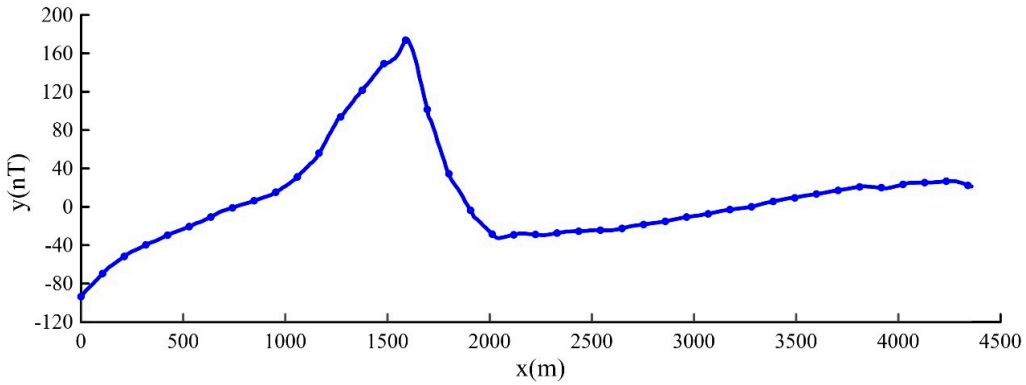

Figure 15. Map of the V anomaly's profile.

4.5.2. Human–Computer Interaction Fitting Inversion

Figure 16 shows the results of the profile inversion fitting of the V anomaly, where the black line represents the original curve of the measured data, and the blue dashed line represents the forward-fitting curve. With a fitting error of 8.01%, the fitting result is well in agreement with the detected magnetic anomaly.

The magnetic geological body, with a magnetic basement which is high in the south and low in the north, forms as a result of the local enrichment of ferromagnetic minerals through hydrothermal activity in the contact zone. The main magnetic anomaly part is a single-peak, positive magnetic anomaly with an amplitude of 190 nT. The fitted magnetic ore is in the shape of an inverted ladder that slopes northward, with no exposures. The overall length of the magnetic geological body is 150 m, with a width of 400 m, and the top of the magnetic geological body is buried at 150 m and the bottom at 300 m. The main body is the middle part of the magnetic body, the thickness which is roughly 120 m. According to the inversion results, the magnetic susceptibility of the magnetic body is $1000 \times 10^{-6} 4\pi$ SI,

which indicates that the prediction in this article is in accord with the practice, and it is one of the possible manifestations of the true underground geological conditions.

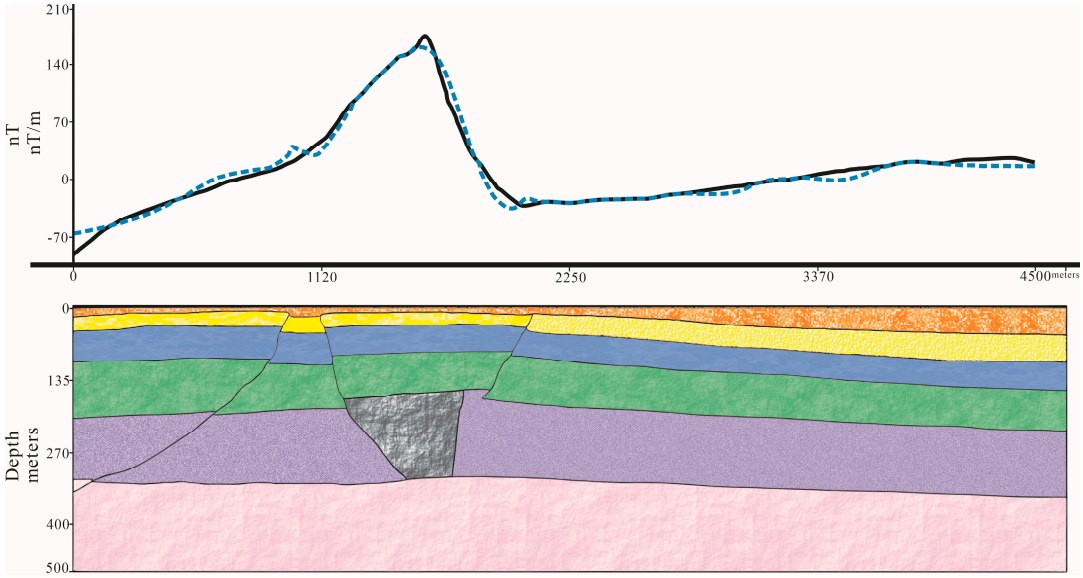

Figure 16. The human–computer interaction fitting inversion (the black line represents the original curve of the measured data, and the blue dashed line represents the forward-fitting curve).

5. Discussion and Conclusions

5.1. Discussion

In this paper, based on the geological information and the geophysical discovery indicators, it is inferred that the V anomaly is a mineral control anomaly, and the particular grounds are as follows:

1. From the point of view of geological ore-searching signs, according to the tectonic location map of the Yichun area (Figure 5) and the regional geological map of the study area (Figure 6), this aeromagnetic study region is located within the Wuxingzhen–Xilin compound fold belt, which belongs to the Yichun–Yanshou polymetallic metallogenic belt. In addition, there are one large iron ore mine and over ten iron and lead–zinc deposits (points) around the study area. Moreover, the intrusive rocks in the study area are predominantly Late Triassic dioritic granites with lead, zinc, and molybdenum anomalies, and the granite generated in this period is magmatic mixed granite. In the study area, Early Cretaceous fine-grained granite occurs sporadically in the form of dykes, and vein rocks are also developed within the area. These factors make it conducive to the later enrichment of elements such as lead, zinc, molybdenum, thereby creating favorable conditions for mineralization.. Additionally, the Late Triassic–Early Jurassic diorite is a landmark intrusive rock for ore-searching in the area, which demonstrates that the geology of the study area possesses favorable conditions for lead and zinc mineralization.
2. Regarding the geophysical ore-searching signs lead–zinc mines have the following aeromagnetic signatures:

- A gently varying weak magnetic field (low, gently positive, negative, or positively and negatively varying magnetic field) as the background field, which typically reflects the mineralizing geological environment (carbonate rocks and acidic and moderately acidic intrusive rocks) of skarn-type deposits (Figure 7b).
- They are typically found around or near strong magnetic anomalies, which may be caused by iron ore or polymetallic iron deposits. Moreover, they are aligned with the spatial distribution of strong magnetic anomalies, indicating that lead–zinc polymetallic deposits are often associated with iron ore or distributed in close proximity.

- The amplitude of the aeromagnetic anomalies of iron polymetallic ores is relatively high, essentially in the range of 550–2500 nT, and several of them are even higher; the aeromagnetic anomalies of lead–zinc polymetallic ores are largely striped or isolated point-like single-peak anomalies (bands), with low and slow peaks, and the amplitude of the anomalies is primarily in the range of 100 nT. The majority of the resolved signals are background noise.
- The majority of AS are weak background fields with isolated anomalies (bands) (Figure 9a). The amplitude is generally 1–2 nT/m, accompanied by iron ore for up to tens of nT/m. Hence, the *V* anomaly was identified as an anomaly in the study area, a single-peaked anomaly (band).

Thus, the *V* anomaly in the study area is defined as a lead–zinc ore anomaly, and the anomaly area should be a primary focus for future exploration of lead–zinc ore.

5.2. Conclusions

- In the Yichun area, there are substantial magnetic differences between the lead–zinc deposits and the surrounding rocks. The dynamic delta wing low-altitude magnetic survey system is characterized by anti-interference and high efficiency and offers clear advantages when locating lead–zinc resources in swamps or forests.
- The Yichun area has seen positive results in exploring lead–zinc resources by applying the low-altitude, high-precision magnetic survey approach. The magnetic basement in the study area is deeper in the north and shallower in the south, with considerable gradient changes. This analysis infers that, in the study area, there are ten linear structures and six rock bodies (veins), pinpointing seven anomaly areas for prospecting, among which the *V* anomaly is identified to be controlling factors-related and the focus of further works.

The lead–zinc mine anomaly (the *V* anomaly) is located in the southeastern part of the study area. It is overall enclosed and in the shape of an oval plane, with a north-west axial orientation. It extends 2.5 km along the strike direction and is about 1.5 km wide, covering an area of 2.8 km^2. The anomaly's intensity varies from −33 nT to 237 nT. Through inversing the anomaly by applying the human–computer interaction fitting method, it can be inferred that the magnetic ore is in the shape of an inverted trapezoidal inclining northward, without any outcrops. The overall length of the magnetic geological body is 150 m, with a width of 400 m, and the top of the magnetic geological body is buried at 150 m and the bottom at 300 m. The main body corresponds to the middle part of the magnetic body, the thickness of which is roughly 120 m. According to the inversion results, the magnetic susceptibility of the magnetic body is $1000 \times 10^{-6} 4\pi$ SI.

This paper conducted a two-dimensional magnetic anomaly inversion within the study area. As the work progresses, subsequent research will be carried out on three-dimensional magnetic anomaly inversion in conjunction with other geophysical methods to achieve a joint inversion method.

Author Contributions: Conceptualization, N.J.; methodology, W.D.; software, N.J. and W.D.; formal analysis, N.J.; resources, X.Q. and Q.S.; writing—original draft preparation, T.Z. and Z.W.; writing—review and editing, Y.L. and H.W.; visualization, W.D. and S.Z.; funding acquisition, W.D. All authors have read and agreed to the published version of the manuscript.

Funding: This research was funded by the National Natural Science Foundation of China with grant number 41904129 and by the Guizhou Provincial 2019 Science and Technology Subsidies with grant number GZ2019SIG.

Data Availability Statement: The data from this study are available from the authors upon request.

Acknowledgments: The authors would like to extend their heartfelt thanks to the two anonymous reviewers for their in-depth review of the manuscript, as well as to the editors for their insightful suggestions and careful revisions.

Conflicts of Interest: The authors declare no conflict of interest.

References

1. Zhu, W.P.; Liu, S.H.; Zhu, H.W.; Xu, L.P. Study on the exploration depth of geophysical methods commonly used. *Prog. Geophys.* **2017**, *32*, 2608–2618. (In Chinese)
2. Malozyomov, B.V.; Martyushev, N.V.; Kukartsev, V.V.; Tynchenko, V.S.; Bukhtoyarov, V.V.; Wu, X.; Tyncheko, Y.A.; Kukartsev, V.A. Overview of Methods for Enhanced Oil Recovery from Conventional and Unconventional Reservoirs. *Energies* **2023**, *16*, 4907. [CrossRef]
3. Benítez, M.E.; Prezzi, C.; Ballivián Justiniano, C.A.; Verdecchia, S.O.; De Martino, F.J.; Carlini, M.; Lanfranchini, M.E. Ground magnetic survey and 3D geophysical model of ultrabasic rocks from the Martín García Complex (Buenos Aires, Argentina). *J. South Am. Earth Sci.* **2023**, *121*, 104117. [CrossRef]
4. Hildenbrand, T.G.; Blakely, R.J.; Hinze, W.J.; Keller, G.R.; Langel, R.A.; Nabighian, M.; Roest, W. Aeromagnetic survey over U.S. to advance geomagnetic research. *Eos Trans. Am. Geophys. Union* **1996**, *77*, 265–268. [CrossRef]
5. Isles, D.J.; Rankin, L.R. *Geological Interpretation of Aeromagnetic Data*; Society of Exploration Geophysicists and Australian Society of Exploration: St. Leonards, NSW, Australia, 2013; ISBN 978-0-643-09809-1.
6. Olakunle, O.O.; Olumuyiwa, A.A.; Adetola, S.O.; Oluwaseyi, E.O. Hydrocarbon potential evaluation of Middle Benue Basin, East Central Nigeria using high resolution aeromagnetic data. *Results Geophys. Sci.* **2023**, *14*, 100058.
7. Mieth, M.; Jokat, W. Banded iron formation at Grunehogna Craton, East Antarctica—Constraints from aeromagnetic data. *Precambrian Res.* **2014**, *250*, 143–150. [CrossRef]
8. Sparlin, M.A.; Lewis, R.D. Interpretation of the magnetic anomaly over the Omaha Oil Field, Gallatin County, Illinois. *Geophysics* **2012**, *59*, 1092–1099. [CrossRef]
9. Spector, A.; Lawler, T.L. Application of aeromagnetic data to mineral potential evaluation in Minnesota. *Geophysics* **2012**, *60*, 1704–1714. [CrossRef]
10. Stephen, O.I.; Aigbedion, I.; Kesyton, O.O.; Musa, A.B. Assessment of groundwater occurrence in a typical schist belt region in Osun State, Southwestern Nigeria using VES, aeromagnetic dataset, remotely sensed data, and MCDA approaches. *Sustain. Water Resour. Manag.* **2022**, *9*, 29.
11. Ahmed, E.; Sultan, A.; Mahmoud, M.; Mahmoud, A.-A. Exploring mineralization zones using remote sensing and aeromagnetic data, West Allaqi Area, Eastern-Desert, Egypt. *Egypt. J. Remote Sens. Space Sci.* **2022**, *25*, 417–433.
12. Cyril, C.O.; John, O.O.; Oyeshomo, A.V.; Gbadebo, O.O. Mineral exploration of Iwo-Apomu Southwestern Nigeria using aeromagnetic and remote sensing. *Egypt. J. Remote Sens. Space Sci.* **2022**, *25*, 371–385.
13. Hodgson, I.; Corporate Publications; Australian Geological Survey Organisation. Airborne Magnetic and Radiometric Surveys. In *AGSO Journal of Australian Geology & Geophysics*; Australian Geological Survey Organisation: Canberra, ACT, Australia, 1997; Volume 17, p. 2, ISSN 1320-1271.
14. Younes, M.; Ahmed, A.; Abdelhalim, M.; Mohammed, O.; Bouchra, D.; Azizi, M.; Yassine, E.-t.; Mohammed, E.A.; Mustapha, B. Aeromagnetic data of the Kelâat M'Gouna inlier (Jbel Saghro, Eastern Anti-Atlas, Morocco): Geotectonic and mining implications. *J. Afr. Earth Sci.* **2023**, *197*, 104744.
15. Lasheen, E.S.R.; Mohamed, W.H.; Ene, A.; Awad, H.A.; Azer, M.K. Implementation of Petrographical and Aeromagnetic Data to Determine Depth and Structural Trend of Homrit Waggat Area, Central Eastern Desert, Egypt. *Appl. Sci.* **2022**, *12*, 8782. [CrossRef]
16. Raana, R.P.; Zeinab, D.; Soumyajit, M.; Leila, H.D.; Tahereh, G.R. Interpretation of aeromagnetic data to detect the deep-seated basement faults in fold thrust belts: NW part of the petroliferous Fars province, Zagros belt, Iran. *Mar. Pet. Geol.* **2021**, *133*, 105292.
17. Tucker, D.H.; Hone, I.G.; Downie, D.; Luyendyk, A.; Horsfall, K.; Anfiloff, V. Aeromagnetic regional survey of onshore Australia. *Geophysics* **2012**, *53*, 254–265. [CrossRef]
18. Huang, L.S.; Jing, R.Z.; Tang, Y.P.; Pei, C.; Zeng, H. Integrated geophysical exploration of Puddy Lake copper nickel mining area, Ontario, Canada. *Miner. Resour. Geol.* **2018**, *32*, 534–539.
19. Eldosouky, A.M.; Elkhateeb, S.O.; Mahdy, A.M.; Saad, A.A.; Fnais, M.S.; Abdelrahman, K.; Andráš, P. Structural analysis and basement topography of Gabal Shilman area, South Eastern Desert of Egypt, using aeromagnetic data. *J. King Saud Univ.-Sci.* **2022**, *34*, 101764. [CrossRef]
20. Lu, N.; Xi, Y.; Zheng, H.; Gao, W.; Li, Y.; Liu, Y.; Cui, Z.; Liao, G.; Liu, J. Development of a Hybrid Fixed-Wing UAV Aeromagnetic Survey System and an Application Study in Chating Deposit. *Minerals* **2023**, *13*, 1094. [CrossRef]
21. Cui, Z.Q.; Xu, Z.L.; Meng, Q.M.; Gao, W.D. Review on exploration effect and characteristics of aeromagnetic survey system based on current three types flying-platform. *Comput. Tech. Geophys. Geochem. Explor.* **2015**, *37*, 437–443.
22. Xi, Y.-Z.; Liao, G.-X.; Lu, N.; Li, Y.-B.; Wu, S. Study on the Aeromagnetic System between Fixed-Wing UAV and Unmanned Helicopter. *Minerals* **2023**, *13*, 700. [CrossRef]
23. Bian, G.; Jin, S.H.; Liu, Q.; Wang, M.N.; Fang, Z.; Sun, C. Application and practice of the powered glider aeromagnetic system in marine magnetisurvey. *Hydrogr. Surv. Charting* **2022**, *42*, 13–16.
24. An, S.L.; Zhou, K.F.; Wang, J.L.; Feng, Q.W. Aeromagnetic survey system with dynamic delta wing and its applications in Kalatage exploration Area. *Prog. Geophys.* **2019**, *34*, 1170–1175.
25. Bona, K.; Soocheol, J.; Eunseok, B.; Seungwook, S.; Seongjun, C. Investigation of Iron Ore Mineral Distribution Using Aero-Magnetic Exploration Techniques: Case Study at Pocheon, Korea. *Minerals* **2021**, *11*, 665.

26. Wang, H.P.; Chen, X.N.; Guo, X.D. Elementary analysis the Anomalies Characteristics of Aeromagnetic and Geomagnetic. *World Nonferrous Met.* **2019**, *volume*, 186–188.
27. Bona, K.; Seulki, L.; Gyesoon, P.; Seong-Jun, C. Development of an Unmanned Airship for Magnetic Exploration. *Explor. Geophys.* **2021**, *52*, 462–467.
28. Ahmed, M.; Mohamed, A.; Fahad, A.; Atef, M.M.; Ahmed, A. Detection of Mineralization Zones Using Aeromagnetic Data. *Appl. Sci.* **2022**, *12*, 9078.
29. Anderson, M.; Matti, J.; Jachens, R. Structural model of the San Bernardino basin, California, from analysis of gravity, aeromagnetic, and seismicity data. *J. Geophys. Res. Solid Earth* **2004**, *109*. [CrossRef]
30. Fuentes–Arreazola, M.A.; Núñez, D.; Cupul–Velázquez, A.M.; Núñez–Cornú, F.J. New insights into El Chichón (Chiapas, Mexico) hydrothermal system from an aeromagnetic survey. *J. S. Am. Earth Sci.* **2023**, *122*, 104169. [CrossRef]
31. Varga, A.; Pozsár, A.; Zajzon, N.; Topa, B.; Benkó, Z.; Pál-Molnár, E.; Raucsik, B. Effects of Metasomatism on Granite-Related Mineral Systems: A Boron-Rich Open Greisen System in the Highiş Granitoids (Apuseni Mountains, Romania). *Minerals* **2023**, *13*, 1083. [CrossRef]
32. Ge, M.H.; Zhang, J.J.; Liu, K.; Wang, M.; Li, M. Petrogenesis of the Late Paleozoic to Mesozoic granite from the Xiao Hinggan Mountains-Zhangguangcai Mountains and its geological implications. *Acta Petrol. Et Mineral.* **2020**, *39*, 385–405.
33. Xu, Z.l.; Meng, Q.M.; Li, W.J.; Cui, Z.Q. The aerogeophysical data processing software system based on Oasis Montaj plateform. *Comput. Tech. Geophys. Geochem. Explor.* **2014**, *36*, 257–261.
34. Sun, B.M.; Wu, Y.G.; Guan, Y.W. Application of joint inversion interpretation of gravity and magnetism in Tianchi deep structure of Changbai Mountain. *Glob. Geol.* **2014**, *33*, 910–915.
35. Li, T.L.; Mu, S.M. The research on the methods of interactive interpretation system for gravity and magnetic data. *J. Chang. Univ. Earth Sci.* **1990**, *03*, 341–346.
36. Reeves, C. *Aeromagnetic Surveys: Principles, Practice and Interpretation*; Geosoft Inc.: Toronto, ON, Canada, 2005.
37. Hinze, W.J.; Frese, R.V.; Saad, A.H. *Gravity and Magnetic Exploration: Principles, Practices, and Applications*; Cambridge University Press: New York, NY, USA, 2013.
38. Han, S.Q.; Wu, G.X.; Zhang, M.H.; Wang, D.P. The structural evolution and prospecting direction of the Yichun Pb, Zn(Ag) metallogenic belt. *Jilin Geol.* **2005**, *04*, 32–36.
39. Liu, Y.M. Metallogenic feature and prospecting signs in Xilin lead-zinc deposit (Erduan-Nangou section), Yichun city, Heilongjiang province. *Miner. Resour. Geol.* **2003**, *S1*, 335–337.
40. Han, Z.X.; Hao, Z.P.; Hou, M. Metallogenic series of ore deposits related to Caledonian granitoids in Xiaohingganling region. *Miner. Depos.* **1995**, *14*, 293–302.
41. Yin, B.C.; Ran, Q.C. Metallogenic evolution in Xiaohingganling-Zhangguangcailing region, Heilongjiang province. *Miner. Depos.* **1997**, *16*, 44–51.
42. Su, Y.M. Geological metallogenic background and prospecting direction of polymetallic deposits in Daxinganling area, Heilongjiang province. *China Resour. Compr. Util.* **2022**, *40*, 55–57+61. [CrossRef]
43. Cai, W.J.; Feng, C.Y.; Ni, W.C.; Shen, Z.X.; Fang, J.Q.; Qiu, C.T.; Yang, J.Z.; Qi, C. Analysis and study of aeromagnetic anomalous characteristics of lead-zinc polymetallic deposits in Yichun area. *Geophys. Geochem. Explor.* **2016**, *40*, 869–875.
44. Zhang, E.; Li, M.S.; Lu, H.X.; Li, H.Y.; Quan, X.D.; Wang, B.; Dong, S.F. Application of Weight Evidence Method to Lead-Zinc Metallogenic Prognosis in Yichun Area, Heilongjiang Province. *J. Jilin Univ. Earth Sci. Ed.* **2017**, *47*, 1419–1428.
45. Pueyo, E.L.; Ayala, C.; Izquierdo-Llavall, E.; Rubio, F.M.; Santolaria, P.; Clariana, P.; Soto, R.; Müller, C.O.; Rey-Moral, C.O.; Zehner, B.; et al. Deliverable 6.4. Optimized 3D reconstruction workflow based on gravimetric, structural and petrophysical data. GEOERA 3DGEO-EU, 3D Geomodeling for Europe, project number GeoE.171.005. Report, 2021, 264p (pp. 103–153). Available online: https://geoera.eu/wp-content/uploads/2021/11/3DGEO-EU_D6.4_Optimized-3D-reconstruction-workflow.pdf (accessed on 31 October 2021).
46. Qi, C.; Cai, W.J.; Tian, Y. Analysis of magnetic susceptibility features of rocks and ores in Xiaoxingan mountain metallogenic belt and application. *Geophys. Geochem. Explor.* **2017**, *8*, 272–281.
47. Xu, L.Y.; Yong, L.W.; Qi, C.A.; Shan, G.; Ning, W.; Jie, W.L.; Cheng, Y. Basin structure and multiresource potential based on high-precision airborne gravity and magnetic data. *Appl. Geophys.* **2022**, *19*, 433–446.
48. Xiong, S.Q.; Tong, J.; Ding, Y.Y.; Li, Z.K. Aeromagnetic data and geological structure of continental China: A review. *Appl. Geophys.* **2016**, *13*, 227–237. [CrossRef]